Zero-Field Dissipationless Chiral Edge Transport and the Nature of Dissipation in the Quantum Anomalous Hall State

Cui-Zu Chang, Weiwei Zhao, Duk Y. Kim, Peng Wei, J. K. Jain, Chaoxing Liu, Moses H. W. Chan, and Jagadeesh S. Moodera

Phys. Rev. Lett. **115**, 057206 — Published 31 July 2015

DOI: 10.1103/PhysRevLett.115.057206

Zero-field dissipationless chiral edge transport and the nature of dissipation in the quantum anomalous Hall state

Cui-Zu Chang[1]*, Weiwei Zhao[2], Duk Y. Kim[2], Peng Wei[1, 3], J. K. Jain[2], Chaoxing Liu[2], Moses H. W. Chan[2]*, and Jagadeesh S. Moodera[1, 3]*

[1]Francis Bitter Magnet Lab, Massachusetts Institute of Technology, Cambridge, MA 02139, USA

[2]The Center for Nanoscale Science and Department of Physics, The Pennsylvania State University, University Park, PA 16802-6300, USA

[3]Department of Physics, Massachusetts Institute of Technology, Cambridge, MA 02139, USA

The quantum anomalous Hall (QAH) effect is predicted to possess, at zero magnetic field, chiral edge channels that conduct spin polarized current without dissipation. While edge channels have been observed in previous experimental studies of the QAH effect, their dissipationless nature at a zero magnetic field has not been convincingly demonstrated. By a comprehensive experimental study of the gate and temperature dependences of local and nonlocal magnetoresistance, we unambiguously establish the dissipationless edge transport. By studying the onset of dissipation, we also identify the origin of dissipative channels and clarify the surprising observation that the critical temperature of the QAH effect is two orders of magnitude smaller than the Curie temperature of ferromagnetism.

Dissipationless edge transport in quantum Hall (QH) effect has resisted technological applications due to the requirements of high magnetic fields and low temperatures [1]. At least one of these two can be circumvented in the so-called quantum anomalous Hall (QAH) state in a ferromagnetic topological insulator (TI), which occurs from the combination of a topologically

non-trivial inverted band structure and an intrinsic spontaneous magnetization (M). The most striking property of QAH state is the presence, at a zero magnetic field, of spin-polarized chiral edge channels that carry current without any dissipation whatsoever [2-4]. In the previously reported QAH state in the Cr-doped TI system [5-8], a sizable longitudinal resistance was observed (at zero magnetic field), possibly as a result of the residual nonchiral dissipative channels [9], thus hampering a direct observation of the dissipationless nature of chiral edge states in nonlocal measurements [6].

In our previous work on V-doped $(Bi,Sb)_2Te_3$, we have observed a robust zero-field quantized Hall plateau accompanied by a negligible longitudinal resistance [10]. However, it had not been unambiguously identified that the dissipationless transport was occurring via chiral edge channels. Furthermore, the physical origin of dissipation has not been clarified. The identification of dissipative channels will be essential in attempts to increase the critical temperature of the QAH state, which is almost two orders of magnitude smaller than the Curie temperature of ferromagnetism in magnetically doped $(Bi,Sb)_2Te_3$ [5-7,10]. To address these issues, we turn to nonlocal transport measurements, which provided definitive experimental evidence for the existence of chiral edge channels in the ordinary QH state at high magnetic fields [1] and also for helical edge channels in the quantum spin Hall (QSH) state at a zero magnetic field [11]. In this *Letter*, we combine two-, three- and four-terminal local and nonlocal measurements to extract information on different conducting channels and directly reveal zero-field dissipationless nature of chiral edge modes and the onset of dissipative channels for the QAH state in V-doped $(Bi,Sb)_2Te_3$.

The four quintuple layers (QL) V-doped $(Bi,Sb)_2Te_3$ films studied here were grown by molecular beam epitaxy (MBE). The transport studies were done using a dilution refrigerator

(Leiden Cryogenics, 10mK, 9T) with the excitation current flowing in the film plane and the magnetic field applied perpendicular to the plane. Six-terminal Hall bridges with bottom-gate electrodes were formed in order to investigate the transport mechanism in detail [10].

We start from local transport measurements for different terminals. **Figure 1(a)** shows the magnetic field ($\mu_0 H$) dependence of the two-terminal resistances, measured at T=25mK, using a bottom gate bias V_g=V_g^0=+7V to reach the charge neutral point. The two-terminal resistances $\rho_{12,12}$, $\rho_{13,13}$ and $\rho_{14,14}$ show exactly h/e^2 quantized values when the magnetization M is well defined. (Note that the first two subscripts of the resistivity refer to the current leads and the last two to the voltage leads.) However, local two-terminal resistance measurement cannot reveal the chirality of the edge transport explicitly.

To probe the detailed flow of the edge channels, we have performed local three-terminal resistance measurements at T=25mK with V_g=V_g^0, as shown in **Figs. 1(d)** to **1(e)**. The resistances $\rho_{14,13}$ and $\rho_{14,12}$ (**Fig.1(d)**) display similar loops that are asymmetric At $\mu_0 H$=0, the $\rho_{14,13}$ and $\rho_{14,12}$ values depend on the magnetization M orientation, with a value of h/e^2 for M>0 and 0 for M<0, respectively. The resistances $\rho_{14,16}$ and $\rho_{14,15}$ display loops that are mirror symmetric to $\rho_{14,12}$ and $\rho_{14,13}$ by $\mu_0 H \rightarrow -\mu_0 H$, as shown in **Fig. 1(e)**. At $\mu_0 H$=0, $\rho_{14,16}$ and $\rho_{14,15}$ are 0 for M>0 and h/e^2 for M<0. The asymmetric loops of three-terminal resistance and the relation between $\rho_{14,16}$ ($\rho_{14,15}$) and $\rho_{14,12}$ ($\rho_{14,13}$) are direct manifestation of the chirality of edge transport, which can be understood from the Landauer-Buttiker formalism [12, 13]. In the QAH regime for M<0, since chiral edge modes propagate anticlockwise ($1 \rightarrow 2 \rightarrow 3 \ldots$), the transmission coefficients, denoted as T_{ij} from electrode *j to i,* are non-zero only for T_{21}=T_{32}=T_{43}=1. When current flows from electrodes 1 to 4 (**Fig. 1(c)**), the voltage distributions are V_2=V_3=V_1=$(h/e^2)I$ and V_6=V_5=V_4=0, where V_i denotes the voltage at the electrode i. Thus, the corresponding resistance

is $\rho_{14,13}=\rho_{14,12}=0$ and $\rho_{14,14}=\rho_{14,16}=\rho_{14,15}=h/e^2$. Likewise for $M>0$, chiral edge modes travel clockwise and the nonzero transmission matrix elements are $T_{61}=T_{56}=T_{45}=1$, leading to the resistance $\rho_{14,14}=\rho_{14,13}=\rho_{14,12}=h/e^2$ and $\rho_{14,16}=\rho_{14,15}=0$. The electrical potential distributions for $M<0$ and $M>0$ (see **Fig. S9**) can also be calculated using the conformal-mapping technique [17]. Hence at $\mu_0 H=0$, the two-terminal resistance $\rho_{14,14}$ is always quantized at h/e^2 regardless of the M orientation. In contrast, the three-terminal local resistances $\rho_{14,13}$ (or $\rho_{14,12}$) and $\rho_{14,15}$ (or $\rho_{14,16}$) depend on the M orientation, as seen in **Figs. 1(d)** and **1(e)**.

Both two- and three-terminal resistances deviate from the quantized value near the coercive fields (H_c) giving rise to two sharp resistance peaks, as shown in **Figs. 1(a), 1(d) and 1(e)**. This corresponds to plateau-to-plateau transition (PPT) region [10]. The heights of the resistance peaks for different terminal measurements are different. We plot the highest resistance values of $\rho_{12,12}$, $\rho_{13,13}$ and $\rho_{14,14}$ as a function of the distance between these terminals, as shown in **Fig. 1(b)**, and find a linear dependence between resistance and distance. This suggests that in the PPT region, the transport is occurring through the bulk of the system [14]. In contrast, the two-terminal resistance of any pair of electrodes is always h/e^2 independent of the length in the QAH regime, which is further consolidated by various quantized rational numbers for different interconnections among the electrodes at the periphery of the six-terminal Hall bridge (see **Figs. S1** and **S2**). This h/e^2 quantized two-terminal resistance is similar to that in QH effect of a two-dimensional electron gas (2DEG) [15,16], with the important distinction that the ballistic edge channels of the QAH state survive without an external magnetic field. Furthermore, the ballistic transport with h/e^2 quantized resistance indicates the propagation of single spin species, in contrast to the QH state for which the spin polarization of the edge channels requires Zeeman coupling to an externally (usually large) applied magnetic field [1].

By comparing local measurement with non-local measurement, we can also reveal distinct behaviors for ballistic chiral edge transport and diffusive bulk transport. In **Fig. 2(a)**, the current was passed through electrodes 3 and 1, while the three-terminal local and nonlocal resistances $\rho_{31,32}$, $\rho_{31,34}$, $\rho_{31,35}$, and $\rho_{31,36}$ were measured at T=25mK with V_g=V_g^0. The $\mu_0 H$ dependence of $\rho_{31,32}$ is also symmetric to those of $\rho_{31,34}$, $\rho_{31,35}$, and $\rho_{31,36}$ (**Fig. 2(b)**) by $\mu_0 H \rightarrow -\mu_0 H$, thanks to the chirality of the edge current. An interesting feature is that $\rho_{31,32}$ and $\rho_{31,36}$ show dramatic peaks in the PPT region with a value of several h/e^2, while $\rho_{31,34}$ and $\rho_{31,35}$ vary between h/e^2 and 0 smoothly without any peaks. The peaks in $\rho_{31,32}$ and $\rho_{31,36}$ are induced by contributions from the local diffusive longitudinal resistance through the bulk. Since no local longitudinal resistances were picked up, no peaks appeared in $\rho_{31,34}$ and $\rho_{31,35}$.

In the above, we have shown that by carefully tuning the V_g, we can achieve, at the lowest temperatures, purely dissipationless chiral edge transport, and the bulk transport only occurs in the PPT region. Next we will explore the origin of dissipation at a zero magnetic field when temperature is increased. We focus on the four-terminal non-local measurement configuration where electrodes 2 and 6 were designated as the current electrodes while electrodes 3 and 5 were used as the voltage probes (**Fig. 3(b)**). Other cases are presented in [14]. In **Figs. 3(a)** and **4(h)**, at the lowest temperature T=25mK, $\rho_{26,35}$ is 0 (in the non-PPT region) regardless of the direction of M, consistent with the picture of a pure chiral edge transport [18]. With increasing temperature, $\rho_{26,35}$ exhibits a hysteresis loop with a decreasing H_c, as shown in **Fig. 3(a)**. The observation of hysteresis, *i.e.* high and low nonlocal resistance states at a higher temperature, indicates the appearance of other dissipative channels besides chiral edge modes. **Figure 3(d)** shows the zero-field non-local signals as a function of temperature, which increase rapidly with temperature up to 2K, accompanied by an increase of longitudinal resistance $\rho_{14,23}$ and a

decrease of Hall resistance $\rho_{14,35}$, as shown in **Fig. 3(c)**. At the same time, the resistance peaks in the PPT region decay rapidly (**Fig. 3(e)**). The different temperature dependences between zero field non-local signals and the resistance peak in the PPT region suggest that they should have different origins. In Fig. 1(b), we have confirmed that the resistance peak in the PPT region follows a linear dependence on distance, thus coming from the bulk carriers. This linearity and the different temperature dependences indicate that the bulk carriers are not responsible for nonlocal signals. A possible explanation comes from the existence of *non-chiral* edge channels, which have been invoked previously to explain a similar hysteresis loop of non-local voltage in Cr doped $(Bi,Sb)_2Te_3$ [6]. In that experiment, however, the hysteresis loop was observed at the lowest temperature, indicating the existence of gapless quasihelical edge modes [9]. For our system, the observation of zero longitudinal and non-local resistances at the lowest temperature (with V_g=V_g^0) rules out gapless modes. Nevertheless, gapped nonchiral edge modes are possible, and, as we argue below, plausible. These non-chiral edge modes originate from two dimensional Dirac surface states on the side surfaces, which are quantized into one dimensional edge modes due to the confinement of finite thickness [9,19].

Our physical picture that the hysteresis loop of non-local signals comes from the coexistence of chiral and non-chiral edge modes finds strong support from the V_g dependence of local and non-local measurements. **Figs. 4(a)** to **4(e)** show longitudinal sheet resistance $\rho_{14,23}$ and Hall resistance $\rho_{14,35}$ at different V_g and the corresponding non-local resistance $\rho_{26,35}$ are shown in **Figs. 4(f)** to **4(j).** A pronounced asymmetry between V_g>V_g^0 and V_g<V_g^0 is observed. At T=25mK with V_g=V_g^0 when the Fermi energy is in the excitation gap, $\rho_{14,35}$ is fully quantized and $\rho_{14,23}$ simultaneously vanishes. The value of non-local resistance $\rho_{26,35}$ is always 0 except at the PPT region (see **Figs. 4(c)** and **4(h)**). For V_g>V_g^0, $\rho_{14,23}$ and $\rho_{14,35}$ have almost no significant change

(**Figs. 4(d)** and **4(e)**), while a hysteresis loop appears for the non-local resistance $\rho_{26,35}$ (**Figs. 4(i)** and **4(j)**). In contrast, for $V_g<V_g^0$, a huge $\rho_{14,23}$ is observed while the non-local resistance $\rho_{26,35}$ is always close to zero (**Figs. 4(f)** and **4(g)**). The variation of $\rho_{14,23}$ and $\rho_{14,35}$, as well as non-local resistance $\rho_{26,35}$, as a function of V_g is summarized in **Figs. 4(k)** and **4(l)**. The ratio between $\rho_{26,35}$ and $\rho_{14,23}$ is around 10^{-2} for $M>0$ in the $V_g>V_g^0$ regime, significantly larger than its value 10^{-5} in the $V_g<V_g^0$ regime, as shown in **Fig. 4(m)**.

The asymmetry between $V_g>V_g^0$ and $V_g<V_g^0$ can be understood from the detailed band structure of $(Bi,Sb)_2Te_3$ and the positioning of the gap relative to the valence and conduction bands. From the previous ARPES measurements [20,21] and the first principles calculations [22,23], it is known that the surface Dirac cones are far away from the bulk conduction band bottom and quite close to (even buried in) the valence band. For our magnetic topological insulator system, the energy spectrum is schematically shown in **Fig. 4(o)**. The green part represents the 2D bulk bands of the thin film, which originates from both the 3D bulk bands and 2D surface bands of top and bottom surfaces. The gap of 2D bulk bands should be determined by the exchange coupling between surface states and magnetization M. Within the 2D bulk gap, there are two types of 1D edge modes: the chiral modes and the non-chiral edge modes originating from surface states of side surfaces as discussed earlier [9,19]. The pure dissipationless chiral edge transport only occurs when the Fermi energy is tuned into the mini-gap of non-chiral edge modes, which is induced by the confinement effect of the side surface [9] and lies close to the maximum of the valence band. For $V_g>V_g^0$, the Fermi energy first cuts through the non-chiral edge modes, leading to a hysteresis loop of non-local resistance due to the coexistence of two types of edge modes. In contrast, for $V_g<V_g^0$, the Fermi energy will first encounter the top of 2D (bulk) valence bands, resulting in a large $\rho_{14,23}$ and an insignificant non-local resistance $\rho_{26,35}$. It is known that

the classical longitudinal transport can also contribute to non-local effect, for which the ratio between non-local resistance $\rho_{26,35}$ and $\rho_{14,23}$ can be estimated as $\frac{\rho_{26,35}^{cl}}{\rho_{14,23}} \approx e^{-\frac{\pi L}{W}}$, where L and W is the length and width of the sample [9]. In our case, $\frac{L}{W} \sim 3$, so this ratio is estimated around 8×10^{-5}, which can explain the observed non-local resistance ratio (10^{-5}) in the $V_g < V_g^0$ regime, but not that (10^{-2}) in the $V_g > V_g^0$ regime. Therefore, non-local signals as well as the hysteresis loop for $V_g > V_g^0$ should be dominated by the mechanism of the coexistence of chiral and non-chiral edge modes.

The above physical picture is also consistent the temperature dependence of longitudinal and non-local resistances in this system. With increasing temperature, $\rho_{14,23}$ increases rapidly (**Fig. 3c**), indicating the existence of bulk carriers. At the same time, the observation of hysteresis loop suggests that non-chiral edge modes should also appear. According to the band dispersion in **Fig. 4(o)**, we speculate that finite temperature excites electrons from 2D valence bands to 1D non-chiral edge channels, so that both 2D bulk holes and 1D non-chiral edge electrons coexist in the system (**Fig 4(n)**). The excitation gap, as indicated in **Fig. 4(o)**, is estimated as 50μeV by fitting temperature dependence of $\rho_{14,23}$, which is consistent with the theoretical prediction [9] and discussed in detail in the supplementary material [14]. This excitation gap is expected to be much smaller than the 2D bulk gap due to magnetization [24] and is consistent with the low critical temperature for the QAH effect. Besides these two kinds of dissipative channels, one should note that other states, such as acceptor or donor states due to impurities, could also exist in the system and cause dissipation.

In summary, our measurements provide a clear and direct confirmation of dissipationless chiral edge transport in the QAH state, identify different types of dissipative channels and

provide insight into why the critical temperature for the QAH effect is two orders of magnitude smaller than the Curie temperature of the ferromagnet. The identification of dissipative channels may suggest ways to increase the critical temperature of the QAH effect, which will be crucial for its use in spintronics as well as for new chiral interconnect technologies [25]. For example, one can consider even thinner film to reduce the number of non-chiral edge modes and increase the mini-gap between non-chiral modes and valence bands. Alternatively, one can also try to reduce the Bi component in the sample to lower the energy of the valence band top, so that all the edge modes can be well above the valence band.

C.Z.C and W.Z. contributed equally to this work. We thank X. Li, H. J. Zhang, M. D. Li, S. C. Zhang and D. Heiman for helpful discussions. J.S.M. and C.Z.C acknowledge support from grants NSF (DMR-1207469), NSF (DMR-0819762) (MIT MRSEC), ONR (N00014-13-1-0301), and the STC Center for Integrated Quantum Materials under NSF grant DMR-1231319. M.H.W.C, W.Z. and D.Y.K. acknowledge support from NSF grants DMR-1420620（Penn State MRSEC) and DMR-1103159. J.K.J. acknowledges support from grant DOE (DE-SC0005042).

***Correspondence to:** czchang@mit.edu(C. Z. C.); chan@phys.psu.edu (M. H. W. C.) and moodera@mit.edu (J. S. M.).

References:

1. C.W.J. Beenakker and H. van Houten, *Solid State Phys.* **44**, 1-228 (1991).

2. X. L. Qi *et al.*, *Phys. Rev. B* **78**, 195424 (2008).

3. R. Yu *et al.*, *Science* **329**, 61 (2010).

4. C. X. Liu *et al.*, *Phys. Rev. Lett.* **101**, 146802 (2008).

5. C. Z. Chang *et al.*, *Science* **340**, 167 (2013).

6. X. Kou *et al.*, *Phys. Rev. Lett.* **113**, 137201 (2014).

7. J. G. Checkelsky *et al.*, *Nat. Phys.* **10**, 731(2014).

8. A. J. Bestwick *et al.*, *Phys. Rev. Lett.* **114**, 187201 (2015).

9. J. Wang *et al.*, *Phys. Rev. Lett.* **111**, 086803 (2013).

10. C. Z. Chang *et al.*, *Nat. Mater.* **14**, 473 (2015).

11. A. Roth *et al.*, *Science* **325**, 294 (2009).

12. M. Buttiker. *Phys. Rev. Lett.* **57**, 1761 (1986).

13. M. Buttiker. *Phys. Rev. B* **38**, 9375 (1988).

14. See Supplementary Materials, which includes Refs. [26] and [27].

15. F. F. Fang and P. J. Stiles, *Phys. Rev. B* **27**, 6487 (1983).

16. F. F. Fang and P. J. Stiles, *Phys. Rev. B* **29**, 3749 (1984).

17. R. W. Rendell and S. M. Girvin, *Phys. Rev. B* **38**, 9375 (1988).

18. S. Datta, *Electron transport in microscopic systems*. Cambridge University Press (1997).

19. R. L. Chu *et al.*, *Phys. Rev. B* **84**, 085312 (2011).

20. J. S. Zhang *et al.*, *Nat. Commun.* **2**, 574 (2011).

21. D. S. Kong *et al.*, *Nat. Nanotechnol.* **6(4)**, 705(2011).

22. G. Wang *et al.*, *Nano Res.* **3(12)**, 874 (2010).

23. H. J. Zhang *et al.*, *Nat. Phys.* **5**, 438(2009).

24. K. He et *al.*, *Natl. Sci. Rev.*1, 39-49 (2014).

25. X. Zhang and S. C. Zhang, *SPIE* **8373**,837309 (2012).

26. S. Komiyama et al., *Phys. Rev. B* **73**, 045333 (2006).

27. K. Ikushima et al., *Phys. Rev. B* **76**, 165323 (2007).

Figures and Figure captions:

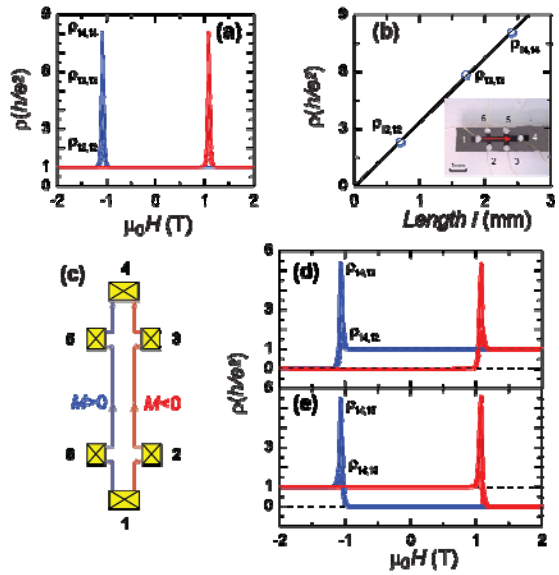

Fig. 1. (color online) Local two-terminal and three-terminal measurements in the QAH regime. (a) Magnetic field ($\mu_0 H$) dependence of two-terminal local resistances $\rho_{12,12}$, $\rho_{13,13}$ and $\rho_{14,14}$. (b) The peak value near the coercive field (H_c) of two-terminal resistances $\rho_{12,12}$, $\rho_{13,13}$ and $\rho_{14,14}$ as a function of the spacing length l(mm) between the voltage electrodes. The inset photograph shows the Hall bridge device. (b) Schematic layout of the device applicable for panels (d) and (e) and also for $\rho_{14,14}$ in (a). The current flows from 1 to 4. The red and blue lines indicates the chiral edge current for magnetization into (M<0) and out of the plane (M>0), respectively. (d, e) $\mu_0 H$ dependence of three-terminal resistances $\rho_{14,13}$, $\rho_{14,12}$ (d) and $\rho_{14,15}$, $\rho_{14,16}$ (e).

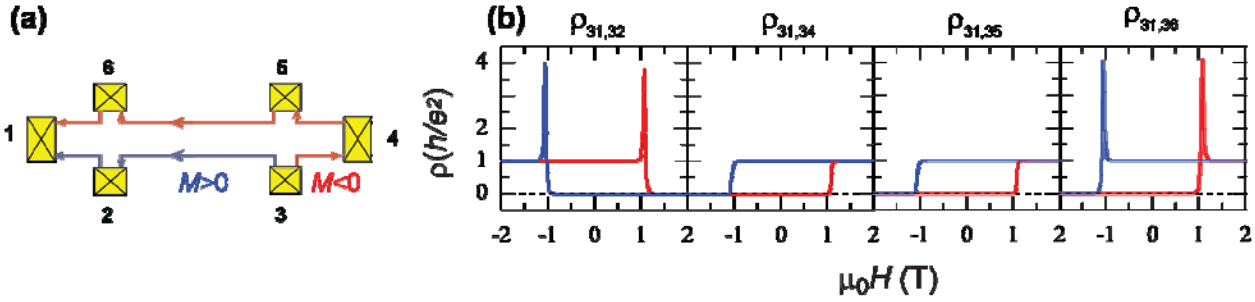

Fig. 2. (color online) Local and nonlocal three-terminal measurements in the QAH regime. (a) Chiral edge conduction channels when the current flows from 3 to 1. (b) $\mu_0 H$ dependence of local and nonlocal three-terminal resistances $\rho_{31,32}$, $\rho_{31,34}$, $\rho_{31,35}$, and $\rho_{31,36}$ measured at T=25 mK with V_g=V_g^0.

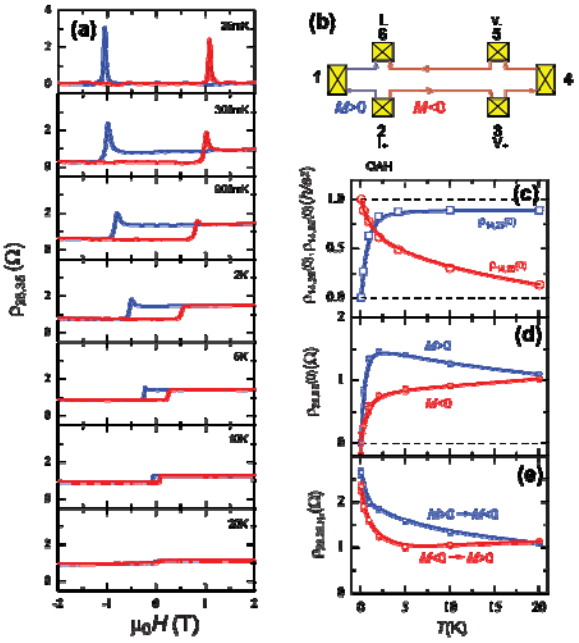

Fig. 3. (color online) Temperature dependence of chiral edge transport in QAH regime. (a) $\mu_0 H$ dependence of the nonlocal resistance $\rho_{26,35}$ measured at V_g=V_g^0 from 25 mK to 20 K. (b) Chiral edge conduction channels when the current flows from 2 to 6, and the nonlocal voltage measured between 3 and 5. (c) Temperature dependence of the zero-field longitudinal sheet resistance $\rho_{14,23}(0)$ (blue curve) and Hall resistance $\rho_{14,35}(0)$ (red curve). (d) Temperature dependence of

zero-field nonlocal signal $\rho_{26,35}(0)$ for $M<0$ (red curve) and $M>0$ (blue curve), respectively. (e) Temperature dependence of nonlocal resistance $\rho_{26,35}$ peaks in the PPT as seen in (a) going between two magnetization orientations.

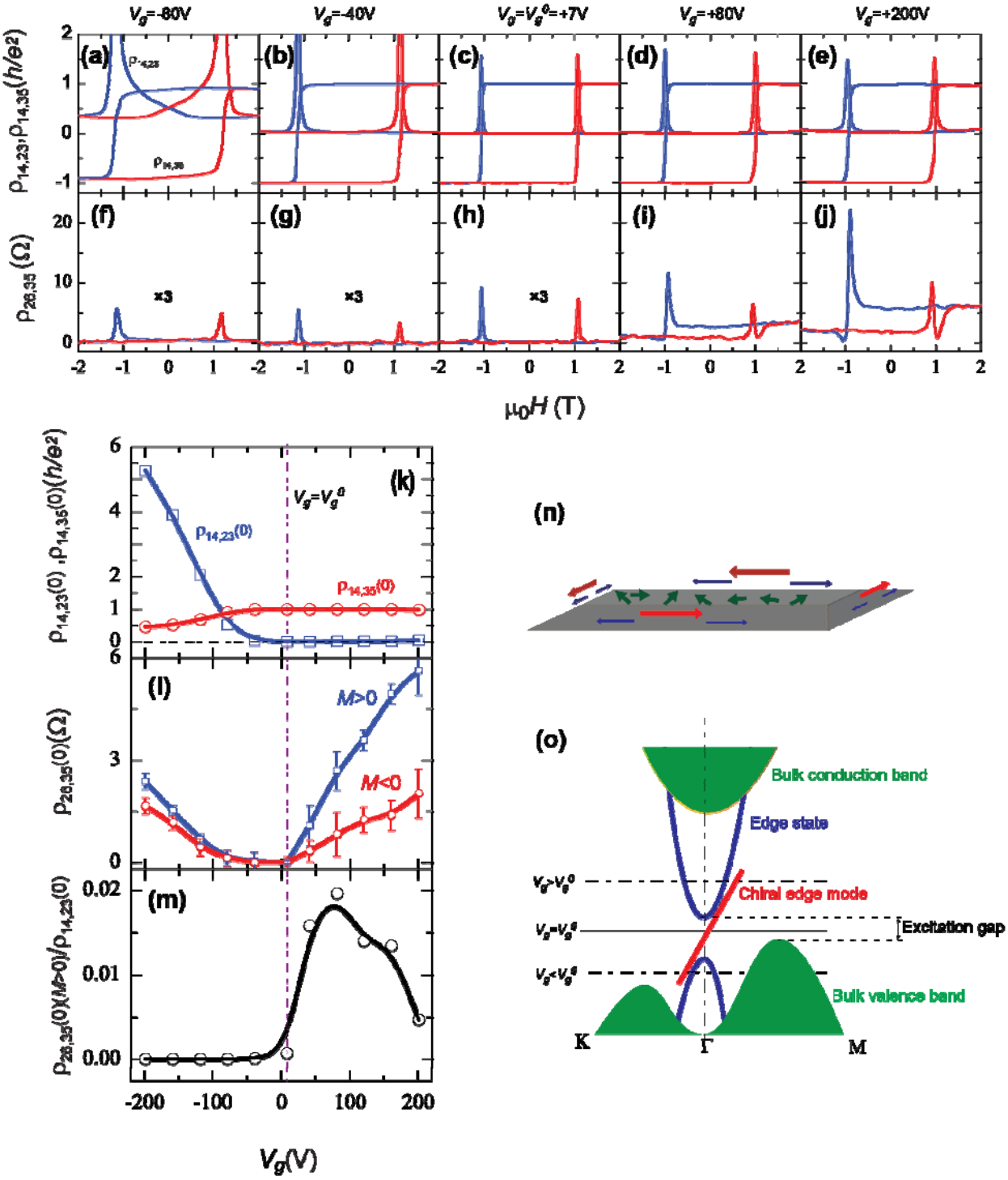

Fig. 4. (color online) Gate bias dependence of chiral edge transport in QAH regime. (a to j) $\mu_0 H$ dependence of longitudinal resistance $\rho_{14,23}$ and Hall resistance $\rho_{14,35}$ (a to e), as well as the

nonlocal signal $\rho_{26,35}$ (f to j) at various V_gs. (k) V_g dependence of the zero-field longitudinal sheet resistance $\rho_{14,23}(0)$ (blue curve) and Hall resistance $\rho_{14,35}(0)$ (red curve). (l) V_g dependence of zero-field nonlocal signal $\rho_{26,35}(0)$ for $M<0$ (red curve) and $M>0$ (blue curve), respectively. (m) V_g dependence of the ratio between non-local resistance $\rho_{26,35}(0)$ for $M>0$ and longitudinal sheet resistance $\rho_{14,23}(0)$. Note that the non-local resistance $\rho_{26,35}(0)$ for $M>0$ indicates that the dissipation channels in the voltage probe side. (n) The schematic diagrams identify three channels in the sample: dissipationless edge channels (red arrows), dissipative edge channels (blue arrows) and dissipative bulk channels (green arrows). (o) The schematic band dispersions of the sample. The horizontal dash-dotted line indicates the Fermi level position for $V_g>V_g^0$ and $V_g<V_g^0$, respectively. The excitation gap is defined as the energy difference between the bottom of the non-chiral edge mode and the maximum of bulk valence band as indicated.